Electrochimica Acta 459 (2023) 142520

Contents lists available at ScienceDirect

Electrochimica Acta

journal homepage: www.journals.elsevier.com/electrochimica-acta

Transport effects in biochip sensors with redox cycling amplification

Tali Dotan [a,b], Michael Nazarenko [b], Yuval Atiya [b], Yosi Shacham-Diamand [a,b,c,*]

[a] Department of Physical Electronics, School of Electrical Engineering, Faculty of Engineering, Tel Aviv University, Tel-Aviv 69978, Israel
[b] Department of Material Science and Engineering, Faculty of Engineering, Tel Aviv University, Tel-Aviv, Israel
[c] TAU/TiET Food Security Center of Excellence (TTFSCoE), Thapar Institute of Engineering and Technology, Patiala, Punjab, India

ARTICLE INFO

Keywords:
Biosensors
Redox cycling
Finite element analysis simulation
Interdigitated electrode array
Mass transport

ABSTRACT

We report a study of transport effects on a microfluidic sensor-chip in which electrochemical sensing is amplified by redox cycling using an interdigitated electrode array (IDA). A full three-dimensional simulation-based model and a simple one-dimensional model for the transition velocity between the two regimes is presented. These models indicate that there exist two dominant regimes: one which is limited by redox cycling diffusion—a unique feature of IDAs— and another which is limited by convection and has dominant flow effects. The transition velocity between the two sensing regimes was found to be $v_{flow}\left[\frac{mm}{sec}\right] = \frac{0.335}{L[\mu m]} + 0.04$ which is similar to the prediction of $v_{flow} \propto \frac{1}{L}$, obtained from the one-dimensional model.

1. Introduction

In the last few decades, and especially after the COVID-19 pandemic, point-of-care diagnostics and field-deployable biosensors have attracted significant attention. Key components of these instruments are microchips that integrate microfluidics with a sensor (e.g., optical or electrochemical) to provide rapid, low-cost, real-time detection of analyte molecules in very small volumes. Electrochemical sensors have been widely used in microband nanofluidic devices [1–4]. They are favored due to small size, low cost, simplicity of use, ease of integration with miniaturized integrated circuits, and their good sensing performance. These sensors provide limits of detection, sensitivity, and selectivity that are suitable for a plethora of applications [5].

Next-generation electrochemical sensors have been miniaturized on solid-state platforms (e.g., arrays and vectors) where the area is limited. However, as the active surface area of the sensors decreases from a few square microns to sub-micron and nanometric scales [6–9], the measured currents drop, hence affecting the limit of detection. As the concentration of many analytes in the physiological environment is low, low signal-to-noise ratios have limited the miniaturization of standard electrochemical sensors.

One way to increase signal at the sensor output is by redox amplification. To achieve amplification, a second working electrode must be incorporated close to the first working electrode and proper bias must be applied to both. Redox amplification can be achieved using nano-gaps [10], enzymatic reactions [11], scanning probes [12], and Coaxial Twin-Electrodes [13] but is usually achieved using an interdigitated electrode array (IDA) [14]. Micrometer-sized interdigitated electrode arrays have been fabricated using robust and scalable processes based on optical lithography and reactive ion-etching techniques [15]. IDA were also previously used for studying the mechanism of electropolymerization [16], the catalytic ability of oxygen reduction reactions and the conductance of conducting polymers [17]. IDAs are commonly integrated in sensors, to enhance their sensitivity [14,18]. IDAs can be integrated into microfluidics, and the physical and electrochemical phenomena that occur in microfluidic channels under flow have been evaluated [19–28].

Bard et al. studied the redox-cycling amplification of a sensor with two working electrodes [29]. They reported that the collection efficiency is strongly dependent on the gap between the two electrodes: As the gap is decreased, the collection efficiency is enhanced. Niwa et al. showed that there is a negative correlation between the collection efficiency and the gap between adjacent electrodes [30].

Redox cycling-based sensors are employed in healthcare, environmental applications, and security monitoring. For example, these sensors have been incorporated into organoids [31] and immunoassays [32, 33], and have also been used to monitor metal ions in drinking water [34]. In all of these devices, the redox amplification is affected by the forced flow. The effect of redox cycling in microfluidic and nanofluidic systems has also been demonstrated. Some studies measured the amplification in the cases with and without flow and showed that the flow itself amplifies the measured electrochemical current, though in

* Corresponding author at: Department of Physical Electronics, School of Electrical Engineering, Faculty of Engineering, Tel Aviv University, Tel-Aviv 69978, Israel.

https://doi.org/10.1016/j.electacta.2023.142520
Received 2 March 2023; Received in revised form 25 April 2023; Accepted 2 May 2023
Available online 3 May 2023
0013-4686/© 2023 Elsevier Ltd. All rights reserved.

most cases, it reduces the amplification factor [35–42].

Analytical and computational modeling provided meaningful insights into the physics of IDAs without requiring numerous device fabrications [7,43–53]. Modeling of the redox cycling phenomenon in IDAs have focused on the effect of array geometry (i.e., the gap between neighboring electrodes and the electrode width) on the amplified currents [29,34,54,55]. Redox cycling under electrolyte flow conditions for a simple 2D model was solved analytically by Compton et al. [21,26], providing deep insights into the fundamental dependence between the gain and the flow conditions. In this work, we applied a more rigorous numerical model of a real device to study the effect of laminar flow on redox cycling. Our results were compared to simple 1D models, and similar functional characteristics were obtained. IDAs with 5–10 μm for both electrodes width and gap were studied numerically and experimentally. The results of the simulations were consistent with those of the physical experiments. The relationship between the two mass transfer methods — diffusion and convection — were analyzed at different flow velocities and for different electrode geometries. Our analyses identified a diffusion-limited regime in which the diffusion mechanisms are dominant, and a flow-dominated regime in which convection affects the limiting current (Fig. 1).

2. Experimental

2.1. Materials and solvents

The laboratory measurements were conducted with 6 mM ferricyanide ($K_3Fe(CN)_6$) in 0.1 M PBS (pH 7.4). All chemicals were obtained from Sigma Aldrich.

2.2. Electrodes

Interdigitated electrode array chips were purchased from MicruX Technologies. The electrodes consist of a 150-nm gold layer with a 50-nm titanium adhesion layer, deposited on a glass substrate, and covered by a SU-8 protective layer. The IDA electrodes were based on a four-electrode system. The working electrode consisted of two individually addressable arrays arranged in a comb structure. The widths of the electrodes were varied between 5 μm and 10 μm, and the inter-comb gap was varied between 5 μm and 10 μm (Table 1). All microelectrodes were 2 mm in length, and the total number of electrode pairs was selected to provide a constant lateral surface area for all IDAs. A quasi-reference Ag/AgCl electrode was fabricated as described previously [56].

2.3. Flow setup

The experiments were performed in a commercial All-in-One cell (MicruX Technologies) with a wall-jet, flow-cell add-on (Fig. 2). The chamber contained an aluminum base with a methacrylate cover and a Poly(methyl methacrylate) (PMMA) batch microcell that was assembled magnetically. The flow was induced by a programmable syringe pump (NE-4000, New Era Pump Systems Inc.) with velocities of 0 to 3 mm/s, corresponding to flow rates of 0–90 μL/min. Before running each experiment, a new IDA chip was taken from an individually sealed package, rinsed with isopropanol and deionized water, and dried under nitrogen flow. The chip was placed in a custom slot and sealed with an O-ring.

2.4. Electrochemical measurements

All single-mode measurements were performed using an IDA chip with a single working electrode connected and a second WE disconnected, an on-chip counter electrode, and an on-chip Quasi-reference AgCl electrode. The dual-mode measurements were performed using a four-electrode setup with two working electrodes.

The different IDAs were electrochemically characterized by cyclic voltammetry (CV) using 6 mM ferricyanide in 0.1 M PBS, pH 7.4 solution. In single working-electrode mode, the potential was cycled between −0.8 V and 1 V (measured with respect to an on-chip AgCl quasi-reference electrode) using a scan rate of 100 mV/s. In dual working-electrode mode, the first working electrode was cycled, and the

Table 1
Electrochemical chip parameters.

Electrode	Electrode width	Inter-comb gap	Number of electrodes
IDA1	10 μm	10 μm	15 pairs
IDA6	5 μm	5 μm	30 pairs

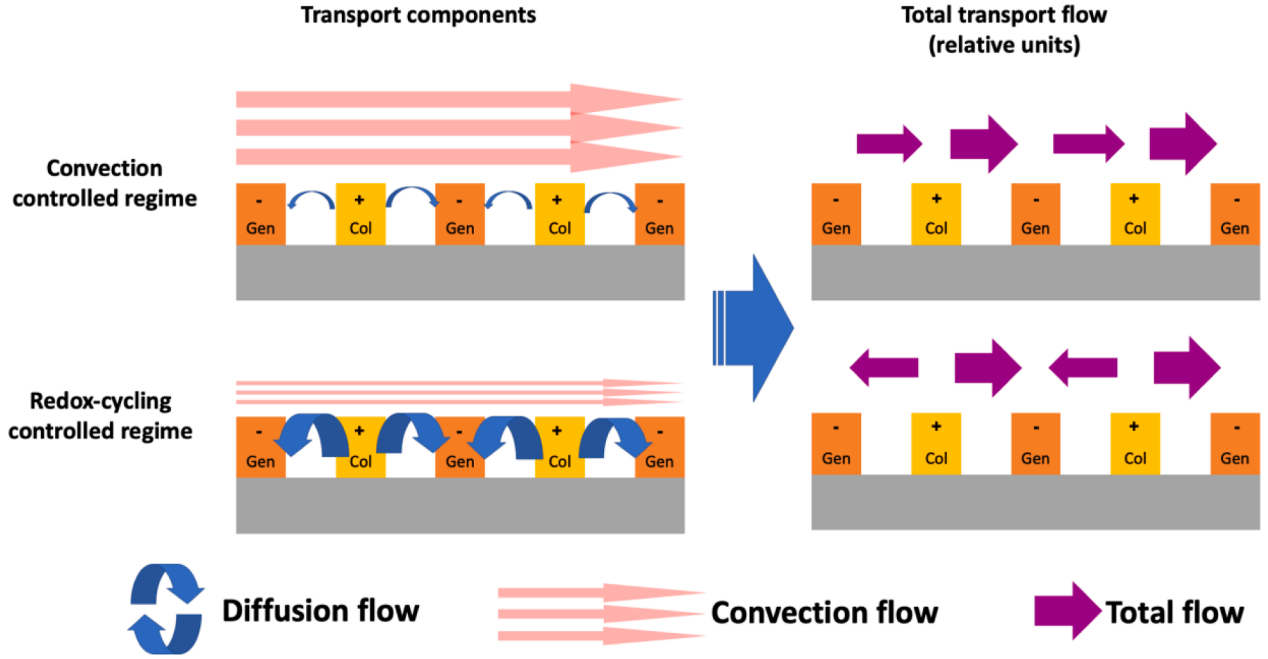


Fig. 1. Schematic of the flow components (diffusion, convection) and total flow in convection-limited (up) and redox-cycling-limited (down) regimes.

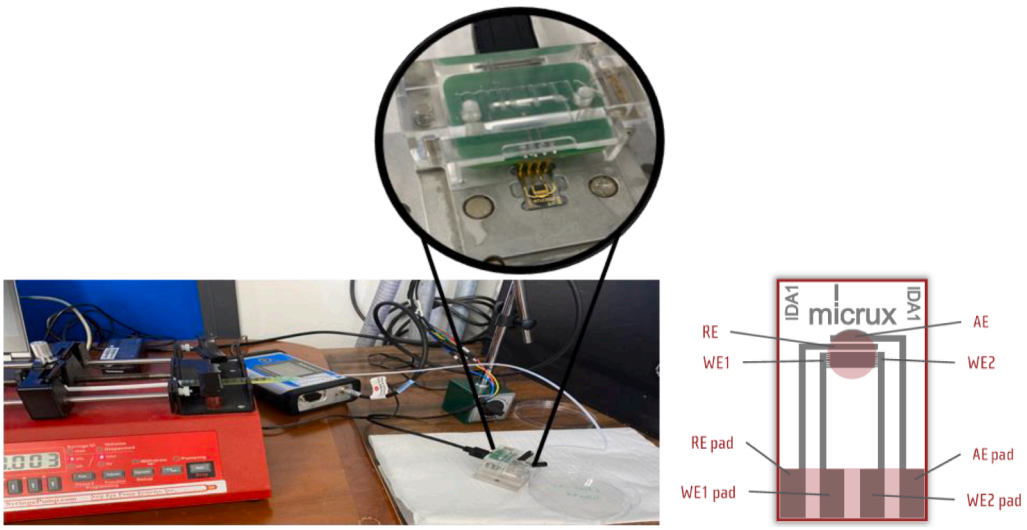


Fig. 2. Experimental setup under forced convection flow (left) and the microfluid chip (right).

second was biased with a constant 1 V potential. Three cycles were typically performed for stabilization, and the data was captured from the second cycle. Each measurement was repeated three to four times and the average value was used for data analysis.

2.5. Finite element simulation

A simulation model was designed to study the electrochemical behavior of the interdigitated electrodes array in single-working-electrode (single mode) and dual-working electrode (dual mode) with and without the effect of forced flow as shown in Fig. 3. The model was built using COMSOL Multiphysics 5.5 with an electrochemistry module. The described geometries were developed starting from a simple, single generator-collector pair model. Subsequently, a model including a real-sized interdigitated microelectrode array was created. Finally, we developed a full model of the microfluidic system and the interdigitated microelectrode array.

3. Theory

A computational simulation model was created supporting the simultaneous electrochemical and forced fluid flow in the microfluidic system. The electrochemical model included the oxidation and reduction of electrochemically active molecules in a redox cycling-based electrochemical sensor system with two working electrodes with different potentials under forced flow. The model included the effects on the electrodes as well as transport phenomena. The modeling started assuming static conditions and then flow modeling was incorporated.

The simulated reaction model is based on the heterogeneous reversible single-electrode oxidation equation:

$$Ox + e^{-} \rightleftharpoons Red \tag{1}$$

Side reactions may also be considered; however, our goal was to test systems with a high level of reversibility (i.e., most of the reduced ions are re-oxidized and vice versa) hence side reactions ignored. According to Kirchhoff's first law, the sum of all the currents entering a node is 0. Since we used two working electrodes, a counter (auxiliary), and the reference electrode current could be neglected, and thus we get:

$$I_{Aux} + I_{WE1} + I_{WE2} = 0 \tag{2}$$

The two working electrode currents are composed of the primary redox cycling current and the secondary currents due to other oxidation/reduction reactions. Neglecting those side reactions, we can assume that the generator and collector currents are the same as the working electrode currents.

The simulation environment was created to mirror the structure of the experimental system which consists of an IDA with two working electrodes integrated and a microfluidic system that provides electrolyte laminar flow on top of the electrodes' surface. The electrical potential of the first working electrode (the generator) was scanned between −1 V and 1 V, and the second working electrode (the collector) was biased with a constant potential of 1 V.

The electrochemical current density, j, at the electrode surface was calculated using the Butler-Volmer equation [57]:

$$j = n{\cdot}F{\cdot}A{\cdot}k_0{\cdot}\left(c_{red}{\cdot}\exp\left(\frac{(1-\alpha)nF\eta}{RT}\right) - c_{ox}{\cdot}\exp\left(\frac{-\alpha nF\eta}{RT}\right)\right) \tag{3}$$

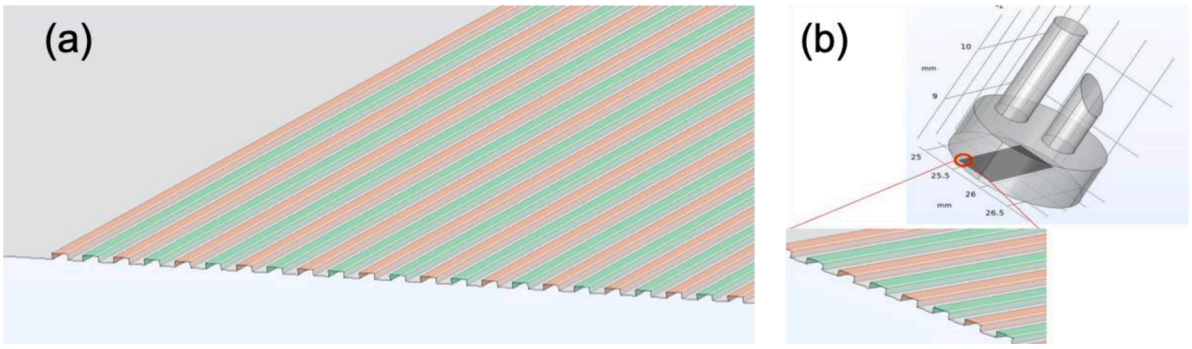


Fig. 3. Schematics of the three simulation configurations. (a) IDA model, and (b) flow cell with IDA.

where n is the number of electrons exchanged, F is the Faraday constant, A is the electrode surface area, k_0 is the heterogeneous rate constant, c_{red} and c_{ox} are the effective concentration of the reduced and oxidized species at the electrode surface, respectively, α is the cathodic charge transfer coefficient, assumed to be 0.5 for a reversible reaction, η is the activation over-potential, R is the universal gas constant; and T is the temperature.

In the static model, the system was modeled assuming that the system is purely controlled by diffusion. From a dynamic condition, the mass transfer at the electrode surface in the perpendicular direction to the electrode length follows the Nernst-Planck equation (Eq. (4)). The right-hand side of this equation describes the three transport phenomena: diffusion, migration, and convection respectively:

$$J = -D\nabla C - \frac{zF}{RT}DC\nabla\Phi + Cv \tag{4}$$

where J is the mass flux, D is the diffusion coefficient of the chemical species, C is its concentration, z is the valence, F is the Faraday constant, R is the universal gas constant, T is the temperature, Φ is the electric potential, and v is the convection velocity. Migration is neglected since at a high concentration of supporting electrolyte and high ionic strength, the electric field outside of the electrical double layer and the mass transfer are both low [58].

Convection mass transfer was studied through simulation and experimentally. During the experiments, the flow was controlled by an electrically controlled syringe pump. The diffusion from the bulk to the electrodes' surface and between adjacent electrodes were modeled by Fick's second law. The I notation refers to a single component (i.e., the reductant and oxidant):

$$\frac{\partial c_i}{\partial t} = D\nabla^2 c_i \tag{5}$$

The normal to the i^{th} component of the flux of species created/deposited at the electrode surface is proportional to current density, J_i, according to Faraday's law of electrolysis:

$$-\vec{n}\cdot J_i = \frac{v_i \cdot i}{nF} \tag{6}$$

Apart from the electrodes and flow inlet/outlet (when applied), the boundaries were insulated to mass transport:

$$-\vec{n}\cdot i = 0 \tag{7}$$

In this work, a two-dimensional cross section of the three-dimensional model was used to calculate the currents. As previously shown [51], a 2D approach provides a good prediction for electrodes that have a length approaching the macroscale since it assumes infinite length and neglects edge effects. The simulation was created in two stages, from a more simplified model to a more detailed design (Fig. 3).

Configuration 1: A three-dimensional model was employed, including a complete IDA surface with a fixed lateral surface area. The number of electrodes in each simulation was derived from the width and the spacings of the design to provide the same total lateral surface area.

Configuration 2: The full flow cell was modeled according to the specific geometry of the flow cell that was provided by the manufacturer. The flow regime was simulated according to the asymmetric design of the flow cell

4. Results and discussion

4.1. Cyclic voltammetry in static mode

Cyclic voltammetry was performed on 6 mM ferricyanide ($K_3Fe(CN)_6$) in 100 mM PBS, pH 7.4 at a scan rate of 100 mV/s in an IDA with electrode width and gap of 5 μm (Fig. 4a). The single-mode voltammogram exhibits a typical duck shape indicative of a reversible reaction with oxidation and reduction peaks. Each peak corresponds to the electron transfer kinetics that control the exponential increase and the mass transfer limited regime that is responsible for the decrease. The dual-mode generator has an anodic sigmoid shape that reflects the pseudo-steady state reached under redox cycling conditions. The collector curve is almost a mirror image of the generator, but absolute value currents are slightly lower due to an imperfect efficiency of the IDA. The dual-mode current is higher than the single-mode current by a factor of 5. The amplification is explained by the redox cycling effect: Every molecule cycles between redox states and shuttles thousands or even millions of times per second between the electrodes, generating an amplified current.

The ferricyanide concentration gradient was simulated in a cross-sectional 2D plane of an IDA (Fig. 4b). The generator electrode acts as the anode where ferrocyanide is formed. The analyte concentration reaches its maximum at the electrode surface and forms a radial molecular diffusion profile. It diffuses to the collector—which acts as the cathode—where it reacts on the surface and is depleted to form ferricyanide.

To provide insight into the effect of IDA dimensions on the redox amplification in our experimental setup, a simulation environment was created using conditions employed in the experiment to model a set of interdigitated electrodes (Configuration 1, Fig. 3a). In the simulation, the electrode gap and width were equal and the total lateral surface area was fixed regardless of electrode gap and width (e.g., if the electrode is twice smaller, there are twice more electrodes). In simulation of the single-mode cyclic voltammogram versus the overpotential value, oxidation and reduction peaks are present due to mass transport limitation at the electrode surface (Fig. 5a). The electron transfer is rapid enough to occur during the forward scan, allowing the detection of the current. However, the analyte concentration at the electrode surface is

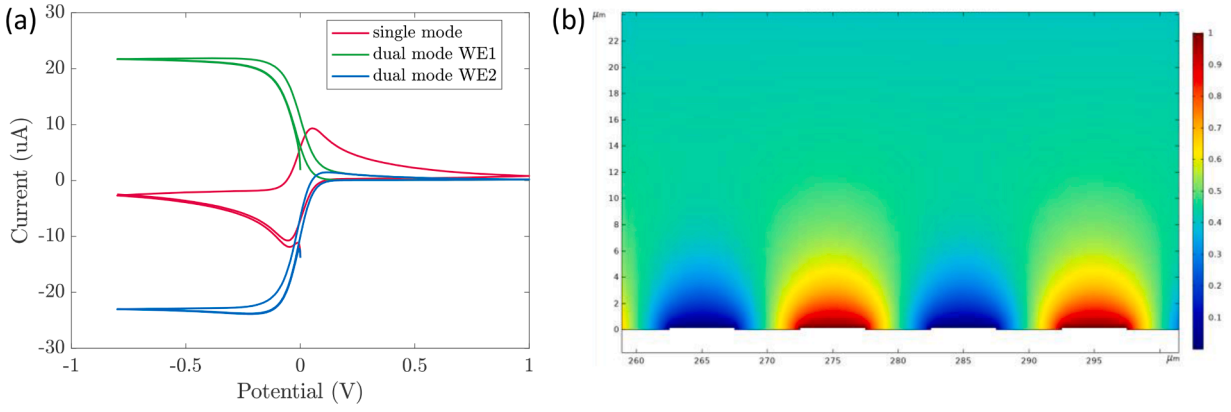


Fig. 4. (a) Single- and dual-mode cyclic voltammograms of 6 mM ferricyanide. (b) Simulated ferricyanide concentration profile under dual-mode configuration.

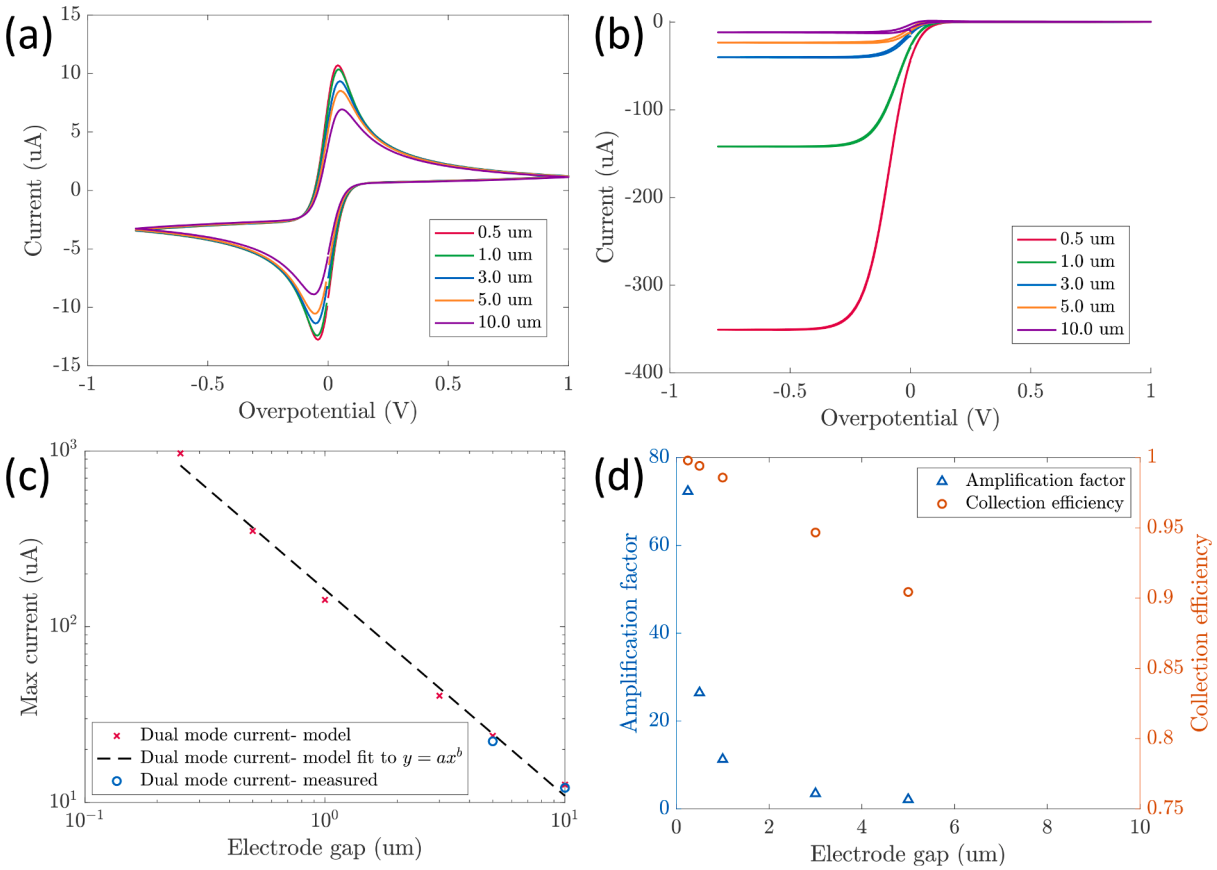


Fig. 5. Static mode simulation. (a) Single-mode (SM) cyclic voltammogram for gaps of 0.5 to 10 μm in an IDA. (b) Dual-mode (DM) generator cyclic voltammogram for gaps of 0.5 to 10 μm in an IDA. (c) Peak dual-mode currents for indicated electrode gaps. (d) Plot of amplification factor versus collection efficiency.

depleted due to the reaction at a higher rate than the diffusion of the analyte toward the electrode, causing the current to decrease. Each curve is a CV of an electrode with a curtain width and gap. The current magnitude is higher for a smaller width and gap. As the number of electrode pairs was adjusted to provide a constant surface coverage regardless of the electrode width, a smaller electrode width and gap effectively had more electrodes, more side edge surface area, and therefore higher current.

When the cyclic voltammogram of the generator electrode in dual mode was computationally obtained at varying electrode widths and gaps, sigmoid shapes were observed at different dimensions, and the signal magnitude increased with a decrease of the dimensions (Fig. 5b). This is consistent with previously published results [55] and is due to the shortening of the diffusion path of the redox species during cycling between IDA electrodes. A plot of peak current of each voltammogram as a function of the electrode gap showed that the simulated currents are consistent with currents that were measured in the lab at 5 and 10 μm (Fig. 5c). The effects of electrode width and electrode gap on redox cycling amplification was previously reported [55]. Assuming a planar IDA where the electrode width is equal to the gap between adjacent electrodes, the limiting current is described by the equation:

$$I_{lim} = 0.47 \cdot \frac{n \cdot F \cdot A \cdot D \cdot C_0}{W_g} \tag{8}$$

where the area is $A = m \cdot l \cdot W_e$, m is the number of digits in the array, l is the length of each digit, n is the number of electrons involved in the redox reaction, F is Faraday's constant, C_0 is the bulk concentration of the redox molecule of interest, D is the diffusion coefficient of the same molecule, and W_e and W_g are the electrode width and gap, respectively. The dependence between the maximum current and the IDA dimension follows the proportion: $i \propto w_g^{-1.17}$ (Fig. 5c), similar to the relationship described by Eq. (8).

Performance parameters depend on the electrode gap (Fig. 5d). When the maximum generator current in dual mode is divided by the maximum current in single mode, the redox amplification factor is obtained, and when the maximum collector current is divided by the maximum generator current, the collection efficiency is obtained. Both the amplification factor and collection efficiency increase as the gap between the electrodes is decreased. Essentially, since the dual-mode current (the numerator) increases drastically with the decrease in dimensions of the IDA, and the single-mode current (the denominator) is only slightly dependent on it, the ratio between these two currents in modes increases drastically with IDA dimensions as well.

The collection efficiency increased when the dimensions of the IDA were decreased, ranging between 80% for 10 μm to over 99% for 1 μm. The amplification factor rapidly increased when the average diffusion length was decreased. For a 1-μm bandwidth and gap, the amplification was 72.

4.2. *Effect of convection flow on the electrochemical current*

The combined effect of redox cycling and convection flow was studied using a controlled flow chamber composed of a syringe pump, a PMMA chamber, and a gold IDA chip with 5 μm gap and electrode width. Additionally, the system was studied computationally (Configuration 2, Fig. 3b). A second model was created based on the static-mode model. In this flow cell, the inlet and the outlet are perpendicular to the electrodes' surface, and are positioned on either side of it (Fig. 6) The electrochemical chip is positioned with the counter electrode towards the inlet, and the working electrodes facing the outlet.

For this flow cell, cyclic voltammograms were simulated at flow

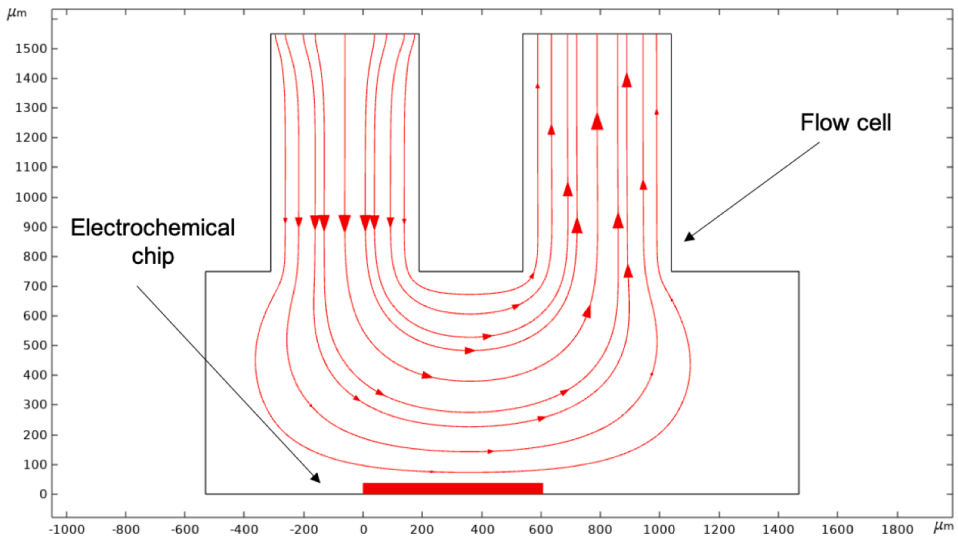


Fig. 6. 2D projection of the 3D stream lines in the microchip.

velocities of 0, 1, and 2 mm/s at 100 mV/s scan rate. In the single mode (Fig. 7a), in a static state with no forced convection flow, the voltammogram shows an anodic and cathodic peak governed by the depletion of the analyte at the electrode surface, faster than its diffusion from the bulk to the electrode. Contrastingly, at higher flow rates, the cyclic voltammogram has a sigmoid shape since the flow chamber provides a constant mass transfer toward the electrode, and concentration saturation is reached

The dual-mode cyclic voltammogram at a static state is a sigmoidal curve. Unlike the single mode, in the dual mode, the analyte concentration reaches a pseudo-steady state where the number of molecules consumed on the electrode surface at a specific time is almost equivalent to the number of molecules generated at the adjacent electrode, which diffuse to the surface. The addition of convection flow in the 1 and 2 mm/s cyclic voltammograms also results in sigmoidal curves. Furthermore, the current magnitude increases with the increase of convection flow velocity. In these cases, the current amplification combines the redox cycling diffusion and the convection flow.

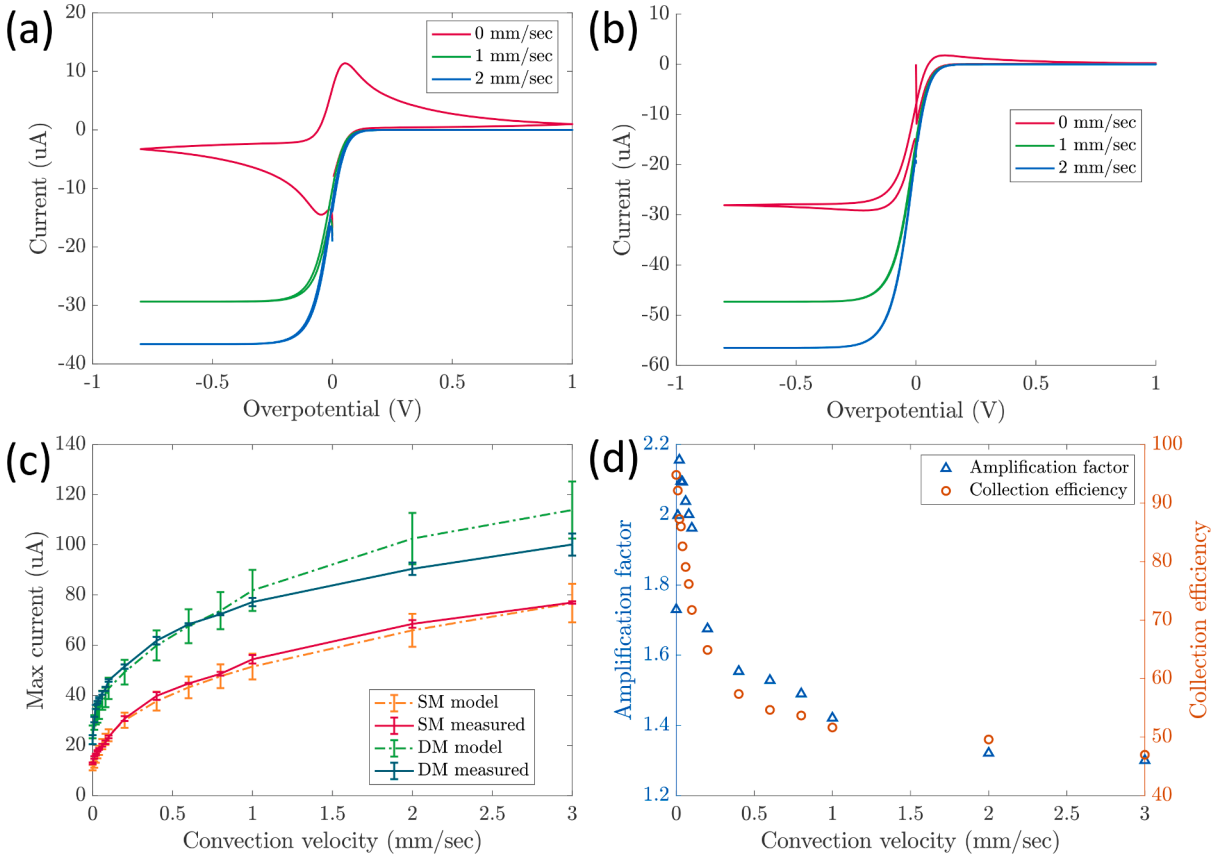


Fig. 7. Dynamic mode simulation. (a) Single-mode (SM) cyclic voltammograms at 0 to 2 mm/s convection flow velocity. (b) Dual-mode (DM) generator cyclic voltammograms at 0 to 2 mm/s convection flow velocity. (c) Peak currents for convection velocity. (d) Amplification factor and collection efficiency.

Single-mode and dual-mode currents increase with velocity, at low velocities with a sharp increase, and at higher velocities, with a smaller increase (Fig. 7c). The maximum currents for single mode and dual mode in a static system for both experimental and simulation measurements are 10 μA and 20 μA, respectively, whereas, for a relatively high flow rate of 3 mm/s, they are almost 80 μA and 100–113 μA, respectively. The dual mode simulated trend is in very good agreement with the experimental results for convection velocities of up to 0.8 mm/s. At higher velocities, the simulated currents are higher by 10% than the experimental ones. The error is most likely attributed to the variation of the viscosity with respect to the room temperature during the measurement. Considering that the simulation assumed a constant room temperature of 25°C, the viscosity in the model is 0.8917 mPa·s [59]. However, since the experiment was conducted without temperature-control, the actual temperature at the measurement environment is 20 and 30°C, correlating to viscosities of 1.005 and 0.797 mPa·s respectively. This +/− 10% variation of viscosity explains *a* +/− 10% deviation of the results.

The dual-mode peak currents are consistently higher than the single-mode peak currents, but at higher velocities, the relative differences between them decrease as can be observed by the amplification factor at Fig. 7d. The redox amplification factors, which are the ratios between the dual-mode and the single-mode currents, as a function of the convection flow velocity were also evaluated (Fig. 7d). Similar to the trend that was shown qualitatively, the amplification factor at a static state where velocity equals zero is above two, and, as the velocity increases, it decreases to values approaching unity. The collection efficiency, which is the collector current divided by the generator current, has efficiency above 90% when the velocity equals zero but decreases with increases in velocity (Fig. 7d). The change in redox cycles and the collection efficiency indicates that when a higher convection field is applied on top of the electrode surface, the relative effect of redox cycling becomes a less dominant factor in the overall electrochemical current.

The limiting currents of electrochemical sensors acting under laminar flow have been studied previously and are dependent on the geometry of the channel for both tubular and planar channel structures [26,57]. Regardless of the geometry, the current is proportional to the cube root of the velocity in the channel. In our simulation, single-mode currents followed the same trend. Fig. 8a shows a logarithmic representation of the relationship between the current and the convection velocity for electrode gaps of 1 to 5 μm. A linear fit of this representation yields slopes of approximately one third (0.320–0.334, Table 2), which is in agreement with the theory presented in Section 3. Furthermore, the relationship between the current and cube root of the velocity yields straight lines starting near the origin with R^2 above 0.99 (Fig. 8b).

In contrast, the dual-mode simulations do not follow the same behavior. In the dual-mode simulations, current increases with an increase of velocity (Fig. 8c), and the relationship between the cube root of the velocity does not follow a straight line and does not intersect with the origin (Fig. 8d). The velocity effect on the generator current can be characterized as a curved line in the logarithmic representation. Two straight lines are extrapolated from the first three data points and the last three, with different slopes. At the lower velocities, the slope is gentle and at higher velocities, the slope is sharper (Table 2). The first slope describes the current behavior at the lower velocities (0.01–0.03 mm/s) and varies between 0.01 and 0.13, increasing for larger dimensions. The second slope describes the current at higher velocities

Table 2
Power law coefficient (RMS errors are less than 1%) for single-mode simulation and for dual-mode simulations for the two slopes 1 and 2, below and above the cross-over velocities, respectively, and cross-over velocities calculated from the 3D and 1D models.

Gap [μm]	Single mode	Dual mode Slope 1	Dual mode Slope 2	Cross Over velocity by 3D model [mm/s]	Cross Over velocity by 1D model [mm/s]
5	0.322	0.132	0.328	0.0707	0.282
3	0.320	0.0651	0.308	0.105	0.471
2	0.322	0.0302	0.286	0.169	0.706
1	0.334	0.0116	0.187	0.335	1.41

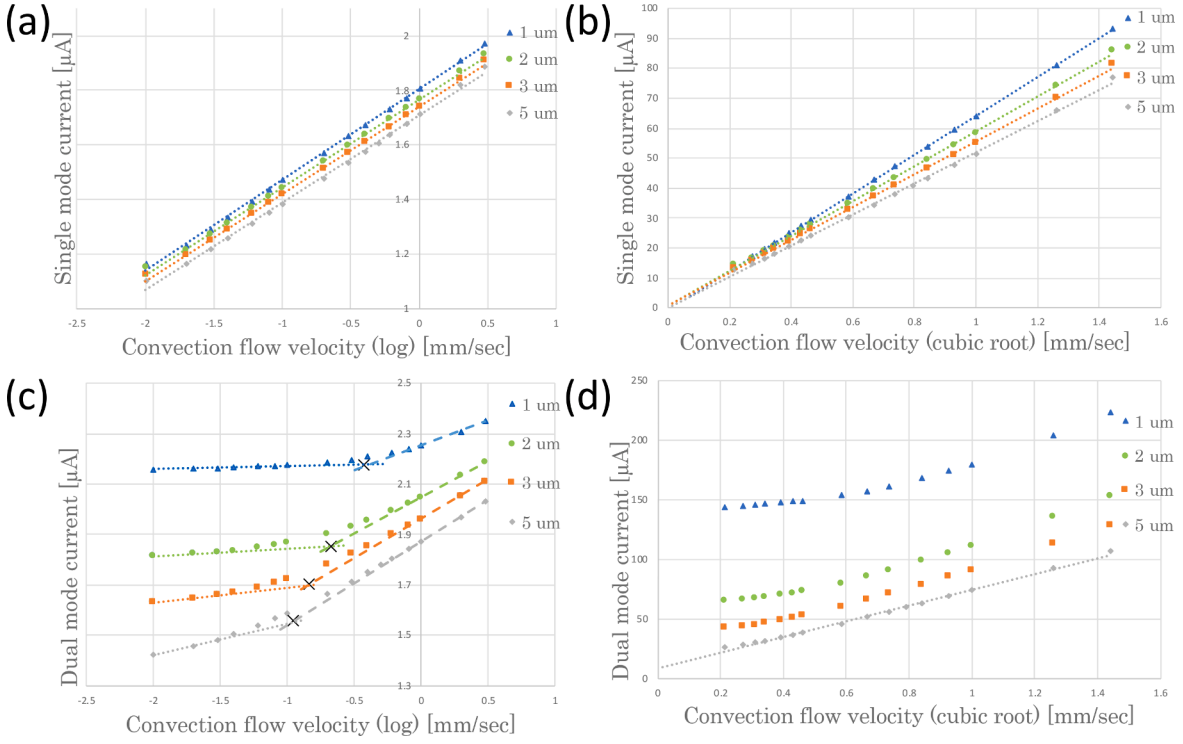


Fig. 8. The effect of convection flow velocity on peak currents. (a) Single-mode dependence in logarithmic scale. (b) Single-mode peak currents as a factor of velocity cubic root. (c) Dual-mode dependence in logarithmic scale. (d) Dual-mode peak currents as a factor of velocity cubic root.

(1–3 mm/s) and ranges between 0.17 and 0.33. For each electrode gap, slope in the high velocity regime is higher than in the redox-cycling regime. As shown in Fig. 7c, the simulated current varies from the experimental measured results by +/− 10%. Therefore, since the slopes are derived from the simulation data, the higher-velocities slopes are also a subject of that variation.

A laminar flow in a channel is influenced by convection, diffusion, and migration phenomena. At relatively low concentrations, the migration flow is neglected and the flow is governed by the simplified form of the Nernst-Planck equation:

$$J = -D\nabla C + Cv. \tag{9}$$

In single mode, the flow is largely controlled by convection as indicated by a slope of 1/3, regardless of the velocity. In the case of dual mode, the current depends on both convection and diffusion. At higher velocities, especially in the case of a larger 5-μm gap where the redox cycling is less dominant, the slope is similar to that of the single mode, and therefore at a very high velocity, the diffusion can be neglected and the convection regime is dominant. At lower velocities, especially in the case of higher redox cycling at a 1-μm gap, the slopes are very small, indicating a weak connection between the forced flow and the current. In this case, the convection can be neglected, and we assume that the regime is redox-cycling controlled.

The inflection point of each curve is defined as the cut point of the two linear approximations. We assume that this point represents the cross-over point between the two straight logarithmic lines (Fig. 8c, Table 2). The value of the cross-over velocity decreases as the electrode spacing increases. It was fitted to a curve $v_{flow} = a{\cdot}L^b + c$, yielding $v_{flow} = \frac{0.335}{L} + 0.04$.

Additionally, an analytical 1D model was developed to determine the cross-over point. It is described as the velocity at which the time required for a single pass of a molecule by convection is equal to the time required for a single pass by diffusion:

$$t_{diffusion} = \frac{L^2}{2D} \equiv t_{convection} = \frac{L}{v} \tag{10}$$

$$v = \frac{2D}{L} \tag{11}$$

where L is the distance between adjacent electrodes, v is the convection velocity, and D is the diffusion coefficient. The inverse relationship between the cross over velocity that was derived from the computational results is similar to the relationship that was calculated from the 1D model, with a constant offset. Assuming an average diffusion coefficient of ferri and ferrocyanide which is $7.06{\cdot}10^{-6}\frac{cm^2}{sec}$[60], the 1D model yields cross over velocities of 0.282 to 1.41 mm/s for electrode width and gap of 5 down to 1 μm respectively (Table 2). These values are higher than the values that were calculated by the 3D model by a factor of 4–4.5, which is most likely attributed to the three-dimensional flow. Thus, there is good agreement between the simulated 3D results and the analytical 1D model.

Our simulation showed that the diffusion layers of each IDA digit change with the convection flow. For the single-mode case, it was previously reported that the faradaic current response is enhanced by a steep concentration gradient compared to purely diffusive mass transport [61]. In dual mode, the phenomena are no longer pure cycling, since the flow is not symmetrical in both directions. In the direction of the convection flow, the total current is the addition of diffusion and convection flow, whereas, in the opposite direction, the total flow is the difference between convection and diffusion.

Concentration profiles were modeled under increasing flow rate conditions (Fig. 9). As expected, the static condition has a hemispherical diffusion field at each IDA digit [9,34,46]. The products of the reaction at the generator mostly often diffuse to the collector electrode and less often diffuse vertically into the bulk solution. With an increase in the convection flow above the electrode surface, the diffusion of the analytes becomes less reciprocal, and the diffusion layer profile becomes directional, directed parallel to the convection flow. Therefore, the reaction product of the generator does not diffuse in both directions according to the applied potential but rather is transported through diffusion and convection to the adjacent electrode downstream. Moreover, the thickness of the diffusion layer decreases with increasing convection flow rate.

5. Conclusions

In this study, we performed both simulations and experiments to characterize an electrochemical sensor based on redox cycling, acting in a flow chamber under laminar flow. We used a static model to examine the impact of the gap between adjacent electrodes in a sensor under static conditions, and showed that the maximum currents in such a sensor act obey $i \propto w_g^{-1.17}$, similar to a previously reported inverse relationship to the distance between the electrodes [55]. We calculated the amplification factor and collection efficiency and showed that they are

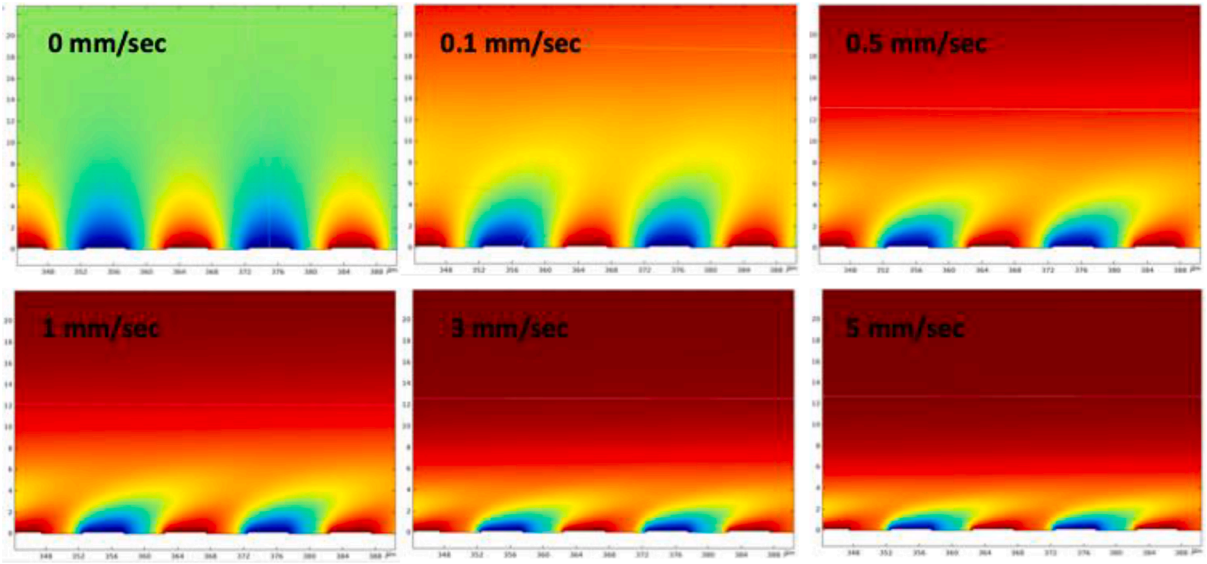


Fig. 9. Concentration profiles without and with flow.

higher when the electrodes are closer together. In an IDA with electrodes of 0.1 μm gap and width, the dual mode current was amplified by a factor of more than 70 compared to the single mode current. In addition, we studied the effect of convection flow velocity on the sensor using a 3D simulation model of the flow chamber used in experimental measurements. We simulated the concentration of chemical species under flow and showed that the diffusion layers shift due to the flow. We showed that the peak currents in single and dual modes increase as the convection flow velocity increases. The peak currents in single mode are proportional to $v^{\frac{1}{3}}$, and the peak currents in dual mode exhibit a dual-regime behavior. At higher velocities, the system is considered to be "convection flow controlled" and the peak currents follow $i \propto v^{0.187}$ to $\propto v^{0.328}$ for electrodes' gap and width of 1 μm to 5 μm respectively. For lower velocities, the system is considered to be "redox cycling controlled" and the peak currents follow $i \propto v^{0.0116}$ to $i \propto v^{0.132}$ for electrodes' gap and width of 1 μm to 5 μm respectively. We observe that for IDAs with larger gaps, the "convection flow controlled" regime approaches single mode behavior as the gaps increase. Similarly, for IDAs with smaller gaps, the "redox cycling controlled" regime approaches the velocity-independent state, i.e. redox cycling in static conditions, as the gaps decrease. The inflection point velocity between the two regimes increases with decreasing the gap between the electrodes. Therefore, the range of the "redox cycling controlled" regime is larger for smaller gaps, and similarly, the "convection flow controlled" regime range is wider for IDAs with larger gaps. A one-dimensional model was used to analytically derive the cross over velocity. The velocity was calculated by the equation $v_{cross-over} = \frac{2D}{L}$, which is very similar equation that was computationally derived by the 3D model $v_{cross-over} = \frac{0.335}{L} + 0.04$, only with a constant offset.

An understanding of the combined effects of redox cycling and convection flow is critical as microfluidic chips with electrochemical sensing amplified by redox cycling using IDAs are becoming widely used in diagnostic assays. The method for prediction of current under any flow rate described here will support technological development of more efficient and accurate devices.

CRediT authorship contribution statement

Tali Dotan: Conceptualization, Simulation, Methodology, Writing. **Michael Nazarenko:** Simulation, Visualization. **Yuval Atiya:** Investigation. **Yosi Shacham-Diamand:** Methodology, Supervision.

Declaration of Competing Interest

The authors declare the following financial interests/personal relationships which may be considered as potential competing interests:

Yosi Shacham- Diamand reports financial support was provided by Israel Innovation Authority. Yosi Shacham-Diamand reports financial support was provided by Israel Science Foundation. Yosi Shacham-Diamand reports financial support was provided by Israel Ministry of Innovation Science & Technology. Tali Dotan reports financial support was provided by Israel Ministry of Innovation Science & Technology.

Data availability

A full model is presented in the supplementary section.

Acknowledgments

This research was funded by the Israel Innovation Authority (IIA) "Biochip" consortium, the Israel Science Foundation administered by the Israel Academy of Science and Humanities grant number 1616/17, the Ministry of Science and Technology grant number 01030360, and the Boris Mints Institute for Strategic Policy Solutions to Global Challenges, the Department of Public Policy, and the Manna centre for Food Security, Tel Aviv University grant number 590351. Ms. Dotan would like to acknowledge the Ministry of Science and Technology STEM fellowship.

Supplementary materials

Supplementary material associated with this article can be found, in the online version, at 10.1016/j.electacta.2023.142520.

References

[1] L.M. Schmidt-Speicher, K. Länge, Microfluidic integration for electrochemical biosensor applications, Curr. Opin. Electrochem. 29 (2021), 100755.
[2] Z. Liu, et al., Electrochemical sensor integrated microfluidic device for sensitive and simultaneous quantification of dopamine and 5-hydroxytryptamine, Sens. Actuators, B Chem. 273 (2018) 873–883.
[3] N. Nesakumar, S. Kesavan, C.Z. Li, S Alwarappan, Microfluidic electrochemical devices for biosensing, J. Anal. Test. 3 (2019) 3–18.
[4] Z.H. Jin, Y.L. Liu, W.T. Fan, W.H. Huang, Integrating flexible electrochemical sensor into microfluidic chip for simulating and monitoring vascular mechanotransduction, Small 16 (2020) 1–5.
[5] Y. Wang, H. Xu, J. Zhang, G. Li, Electrochemical sensors for clinic analysis, Sensors 8 (2008) 2043–2081.
[6] J.I. Heo, et al., Carbon interdigitated array nanoelectrodes for electrochemical applications, J. Electrochem. Soc. 158 (2011) J76.
[7] N. Alayo, et al., Gold interdigitated nanoelectrodes as a sensitive analytical tool for selective detection of electroactive species via redox cycling, Microchim. Acta 183 (2016) 1633–1639.
[8] K. Ueno, M. Hayashida, J.Y. Ye, H Misawa, Fabrication and electrochemical characterization of interdigitated nanoelectrode arrays, Electrochem. Commun. 7 (2005) 161–165.
[9] P. Tomčík, Microelectrode arrays with overlapped diffusion layers as electroanalytical detectors: theory and basic applications, Sensors (Switzerland) 13 (2013) 13659–13684.
[10] H.S. White, K McKelvey, Redox cycling in nanogap electrochemical cells, Curr. Opin. Electrochem. 7 (2018) 48–53.
[11] H. Yang, Enzyme-based ultrasensitive electrochemical biosensors, Curr. Opin. Chem. Biol. 16 (2012) 422–428.
[12] R.C. Engstrom, M. Weber, D.J. Wunder, R. Burgess, S Winquist, Measurements within the diffusion layer using a microelectrode probe, Anal. Chem. 58 (1986) 844–848.
[13] T. Šafarik, et al., Bottom-up designed porous coaxial twin-electrodes for efficient redox cycling, Adv. Funct. Mater. 33 (2023), 2210638.
[14] J.S. Borchers, C.R. Campbell, S.B. Van Scoy, M.J. Clark, R.K. Anand, Redox cycling at an array of interdigitated bipolar electrodes for enhanced sensitivity in biosensing**, ChemElectroChem 8 (2021) 3482–3491.
[15] S. Partel, et al., Lift-off free fabrication approach for periodic structures with tunable nano gaps for interdigitated electrode arrays, ACS Nano 10 (2016) 1086–1092.
[16] K. Murugappan, M.R Castell, Bridging electrode gaps with conducting polymers around the electrical percolation threshold, Electrochem. Commun. 87 (2018) 40–43.
[17] G. Salinas, B.A. Frontana-Uribe, Analysis of conjugated polymers conductivity by in situ electrochemical-conductance method, ChemElectroChem 6 (2019) 4105–4117.
[18] T.M. Swager, 50th anniversary perspective: conducting/semiconducting conjugated polymers. A personal perspective on the past and the future, Macromolecules 50 (2017) 4867–4886.
[19] J.A. Alden, R.G. Compton, Hydrodynamic voltammetry with channel microband electrodes: axial diffusion effects, J. Electroanal. Chem. 404 (1996) 27–35.
[20] A.B. Miles, R.G Compton, Theory of square wave voltammetry at uniformly accessible hydrodynamic electrodes, J. Electroanal. Chem. 487 (2000) 75–89.
[21] M.J. Bidwell, J.A. Alden, R.G. Compton, Hydrodynamic voltammetry with channel microband electrodes: the simulation of voltammetric waveshapes, J. Electroanal. Chem. 417 (1996) 119–128.
[22] Compton, R.G. & Winkler, J. Hydrodynamic voltammetry with. 5029–5034 (1995).
[23] R.G. Compton, R.G. Wellington, Spectrofluorimetric hydrodynamic voltammetry: the investigation of electrode reaction mechanisms, J. Phys. Chem. 98 (1994) 270–273.
[24] R.G. Compton, et al., Hydrodynamic voltammetry with channel microband electrodes: potential step transients, J. Phys. Chem. 98 (1994) 1270–1275.
[25] R.G. Compton, J. Winkler, D.J. Riley, S.D. Bearpark, Spectrofluorimetric hydrodynamic voltammetry: investigation of reactions at solid/liquid interfaces, J. Phys. Chem. 98 (1994) 6818–6825.
[26] R.G. Compton, A.C. Fisher, R. Geoffrey Wellington, P.J. Dobson, P.A. Leigh, Hydrodynamic voltammetry with microelectrodes. Channel microband electrodes: theory and experiment, J. Phys. Chem. 97 (1993) 10410–10415.
[27] R.G. Compton, A.C. Fisher, R.G. Wellington, J. Winkler, Spectrofluorimetric hydrodynamic voltammetry: theory and practice, J. Phys. Chem. 96 (1992) 8153–8157.

[28] N.V. Rees, R.G. Compton, Hydrodynamic microelectrode voltammetry, Russ. J. Electrochem. 44 (2008) 368–389.
[29] A.J. Bard, T.V. Shea, J.A. Crayston, G.P. Kittlesen, M.S. Wrighton, Digital simulation of the measured electrochemical response of reversible redox couples at microelectrode arrays: consequences arising from closely spaced ultramicroelectrodes, Anal. Chem. 58 (1986) 2321–2331.
[30] O. Niwa, M. Morita, H. Tabei, Electrochemical behavior of reversible redox species at interdigitated array electrodes with different geometries: consideration of redox cycling and collection efficiency, Anal. Chem. 62 (1990) 447–452.
[31] C. Zanetti, et al., Monitoring the neurotransmitter release of human midbrain organoids using a redox cycling microsensor as a novel tool for personalized Parkinson's disease modelling and drug screening, Analyst 146 (2021) 2358–2367.
[32] Z. Chen, H. Wang, Z. Zhang, L Chen, Chemical redox-cycling for improving the sensitivity of colorimetric enzyme-linked immunosorbent assay, Anal. Chem. 91 (2019) 1254–1259.
[33] G.Y. Lee, et al., Chronoamperometry-based redox cycling for application to immunoassays, ACS Sens. 3 (2018) 106–112.
[34] A.J.C. Wahl, et al., Diffusion profile simulations and enhanced iron sensing in generator-collector mode at interdigitated nanowire electrode arrays, Electrochim. Acta 277 (2018) 235–243.
[35] A. Aoki, T. Matsue, I Uchida, Electrochemical response at microarray electrodes in flowing streams and determination of catecholamines, Anal. Chem. 62 (1990) 2206–2210.
[36] K. Ueno, H.B. Kim, N Kitamura, Characteristic electrochemical responses of polymer microchannel-microelectrode chips, Anal. Chem. 75 (2003) 2086–2091.
[37] B. Wolfrum, M. Zevenbergen, S Lemay, Nanofluidic redox cycling amplification for the selective detection of catechol, Anal. Chem. 80 (2008) 972–977.
[38] E.D. Goluch, B. Wolfrum, P.S. Singh, M.A.G. Zevenbergen, S.G Lemay, Redox cycling in nanofluidic channels using interdigitated electrodes, Anal. Bioanal. Chem. 394 (2009) 447–456.
[39] S. Kang, K. Mathwig, S.G. Lemay, Response time of nanofluidic electrochemical sensors, Lab Chip 12 (2012) 1262–1267.
[40] T.H. Kim, et al., Flow-enhanced electrochemical immunosensors on centrifugal microfluidic platforms, Lab Chip 13 (2013) 3747–3754.
[41] R.R. Kamath, M.J Madou, Three-dimensional carbon interdigitated electrode arrays for redox-amplification, Anal. Chem. 86 (2014) 2963–2971.
[42] V. Matylitskaya, S. Kasemann, G. Urban, C. Dincer, S Partel, Electrochemical characterization of nanogap interdigitated electrode arrays for lab-on-a-chip applications, J. Electrochem. Soc. 165 (2018) B127–B134.
[43] H. Kwon, E. Akyiano, Simulation of cyclic voltammetry of ferrocyanide/ferricyanide redox reaction in the EQCM Sensor, Comsol.De 2–6 (2011).
[44] K.V. Singh, et al., 3D nanogap interdigitated electrode array biosensors, Anal. Bioanal. Chem. 397 (2010) 1493–1502.
[45] J. Strutwolf, D.E. Williams, Electrochemical sensor design using coplanar and elevated interdigitated array electrodes. A computational study, Electroanalysis 17 (2005) 169–177.
[46] A. Wahl, et al., Gold nanowire electrodes in array: simulation study and experiments, Faraday Discuss. 164 (2013) 377–390.
[47] E. Kätelhön, K.J. Krause, P.S. Singh, S.G. Lemay, B. Wolfrum, Noise characteristics of nanoscaled redox-cycling sensors: investigations based on random walks, J. Am. Chem. Soc. 135 (2013) 8874–8881.
[48] D. Han, Y.R. Kim, C.M. Kang, T.D. Chung, Electrochemical signal amplification for immunosensor based on 3D interdigitated array electrodes, Anal. Chem. 86 (2014) 5991–5998.
[49] M.J.J. Van Megen, J.G. Bomer, W. Olthuis, A Van Den Berg, Solid state nanogaps for electrochemical detection fabricated using edge lithography, Microelectron. Eng. 115 (2014) 21–25.
[50] G.Y. Lee, et al., Redox cycling-based immunoassay for detection of carcinogenic embryonic antigen, Anal. Chim. Acta 971 (2017) 33–39.
[51] B. O'Sullivan, et al., A direct comparison of 2D versus 3D diffusion analysis at nanowire electrodes: a finite element analysis and experimental study, Electrochim. Acta 408 (2022), 139890.
[52] D. Butler, A Ebrahimi, Rapid and sensitive detection of viral particles by coupling redox cycling and electrophoretic enrichment, Biosens. Bioelectron. 208 (2022), 114198.
[53] M. Odijk, W. Olthuis, V.A.T. Dam, A Van Den Berg, Simulation of redox-cycling phenomena at interdigitated array (IDA) electrodes: amplification and selectivity, Electroanalysis 20 (2008) 463–468.
[54] U. Ghia, K.N. Ghia, C.T Shin, High-*Re* solutions for incompressible flow using the Navier-Stokes equations and a multigrid method, J. Comput. Phys. 48 (1982) 387–411.
[55] K. Aoki, M. Morita, O. Niwa, H Tabei, Quantitative analysis of reversible diffusion-controlled currents of redox soluble species at interdigitated array electrodes under steady-state conditions, J. Electroanal. Chem. 256 (1988) 269–282.
[56] R. Popovtzer, T. Neufeld, E.z. Ron, J. Rishpon, Y. Shacham-Diamand, Electrochemical detection of biological reactions using a novel nano-bio-chip array, Sens. Actuators, B Chem 119 (2006) 664–672.
[57] A.J. Bard, L.R. Faulkner, Electrochemical methods fundamentals and applications, Compr. Sampl. Sample Prep. 2 (2012) 135.
[58] K. Ngamchuea, C. Batchelor-McAuley, R.G. Compton, Anodic stripping voltammetry of silver in the absence of electrolytes: theory and experiment, J. Electroanal. Chem. 830–831 (2018) 122–130.
[59] J. Kestin, M. Sokolov, W.A. Wakeham, Viscosity of liquid water in the range− 8 C to 150 C, J. Phys. Chem. Ref. Data 7 (1978) 941–948.
[60] J.E. O'Reilly, Oxidation-reduction potential of the ferro-ferricyanide system in buffer solutions, BBA - Bioenergy 292 (1973) 509–515.
[61] L. Rassaei, K. Mathwig, E.D. Goluch, S.G Lemay, Hydrodynamic voltammetry with nanogap electrodes, J. Phys. Chem. C 116 (2012) 10913–10916.